Journal of the European Ceramic Society 46 (2026) 117891

Contents lists available at ScienceDirect

Journal of the European Ceramic Society

journal homepage: www.elsevier.com/locate/jeurceramsoc

Effect of atmosphere on thermal debinding of DLP-printed ceramics

Premysl Stastny [a], Ondrej Man [a], Dominik Brouczek [b], Martin Schwentenwein [b], Martin Trunec [a,c,*]

[a] CEITEC BUT, Brno University of Technology, Purkynova 123, Brno 612 00, Czech Republic
[b] Lithoz GmbH, Mollardgasse 85a/2/64-69, Vienna 1060, Austria
[c] Institute of Materials Science and Engineering, Brno University of Technology, Technicka 2, Brno 616 69, Czech Republic

ARTICLE INFO

Keywords:
3D printing
Binder removal
Microstructure
Size limit
Cracking

ABSTRACT

This study investigates the effect of the gas atmosphere on the size limit for defect-free thermal binder removal in 3D-printed alumina bodies fabricated using digital light processing (DLP). Binder removal from cylindrical specimens with diameters ranging from 5 mm to 15 mm was carried out in either nitrogen or air atmospheres under different heating schedules. In nitrogen, defect-free debinding was achieved for specimens up to 15 mm in diameter. In contrast, defect-free binder removal in air was limited to specimens as small as 5 mm. Thermogravimetric analysis and microstructural characterization were employed to elucidate the role of the atmosphere in binder removal and defect formation. Microstructural differences between debinding in air and nitrogen were identified. Based on these results, mechanisms of binder removal in ceramic DLP printed bodies with acrylate-based crosslinked binder systems are proposed, and critical steps for achieving defect-free processing are discussed.

1. Introduction

Additive manufacturing (AM) of ceramics, also known as three-dimensional (3D) ceramic printing, is experiencing a huge interest in both academic and industrial communities because of promising results in the production of high-performance ceramic components with geometrically complex architectures, which are difficult to fabricate using traditional processing methods [1–3]. Among the various AM technologies, vat photopolymerization methods, e.g., stereolithography (SLA) or digital light processing (DLP), are considered to be the most promising technologies due to their excellent feature resolution and quality of the final parts [4]. Regardless of the vat photopolymerization method used, the photopolymerization of photosensitive resins containing dispersed ceramic particles is the characteristic processing step [5]. After illuminating the photosensitive ceramic suspension with an appropriate wavelength light source, a complex polymeric network is formed, and the liquid ceramic suspension is transformed into a solid layer. As these layers are stacked on top of each other, the final 3D part is formed. The 3D-printed ceramic part is then composed of ceramic particles anchored in a polymeric network [6]. Before sintering, the polymeric network and all other organic additives must be removed in a separate binder removal (debinding) step. Removal of the polymeric network is considered as one of the most critical steps in the process chain. Various advanced debinding methods have been developed for photopolymerized 3D printed parts, such as microwave-assisted debinding [7], solvent debinding [8], supercritical CO_2 debinding [9]. However, thermal debinding [10] is still the most common binder removal method. This step usually takes more time than the printing step itself and can result in defect formation [10]. Once the defects are created in the body during debinding, they cannot by fully healed in subsequent steps, and the defects tend to enlarge during sintering. The occurrence of debinding defects increases with the increased wall thickness of the printed body. Several authors have published research on the maximum obtainable wall thickness without defects. Depending on the composition of the ceramic slurry, the part design, and the debinding conditions (e.g., heating schedule and gas atmosphere), the maximum thickness ranged from 5 mm to 12 mm [11–13].

The mechanisms of thermal debinding include thermal degradation of the polymeric network, diffusion of degradation products and other low-molecular-weight binder additives to the surface of the body (or the binder/atmosphere interface), and their evaporation [14,15]. In an air atmosphere, an additional degradation mechanism, namely oxidative degradation, is involved [14,16]. Abrupt gas evolution due to the boiling of low molecular weight components and degradation products in the

* Correspondence to: Central European Institute of Technology, Brno University of Technology, Purkynova 123, Brno 612 00, Czech Republic
E-mail address: martin.trunec@ceitec.vutbr.cz (M. Trunec).

https://doi.org/10.1016/j.jeurceramsoc.2025.117891
Received 17 July 2025; Received in revised form 7 October 2025; Accepted 8 October 2025
Available online 10 October 2025

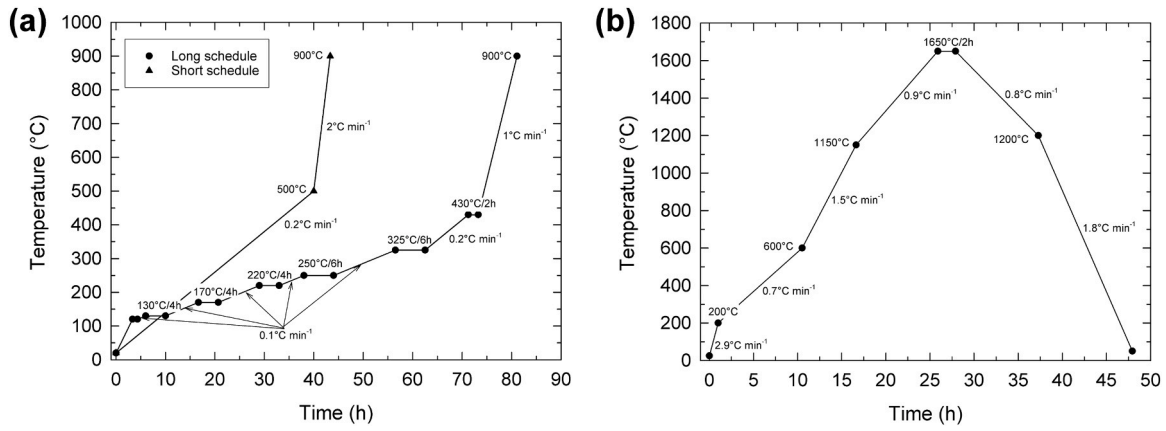

Fig. 1. Heating schedule for (a) debinding and (b) sintering of printed samples.

pores filled with a liquid/solid binder is considered to be one of the main causes of defect formation during thermal debinding [10,14,17,18]. A common approach to preventing defect formation during debinding is to use low heating rates (as low as 0.1–0.2 °C min^{-1}) and to include dwell periods of several hours in temperature ranges associated with high mass loss rates [13,18,19]. Thermogravimetric analysis (TGA) and differential scanning calorimetry (DSC) of the printed material are typically employed to identify the critical temperature ranges associated with high mass loss rates and intensive degradation reactions [10]. Recent reports also demonstrate the importance of the debinding atmosphere. Many authors reported stronger internal stresses and more serious defect formation during debinding in an air atmosphere than in non-oxidizing atmospheres, such as Ar [19], 95 % Ar + 5 % H_2 [20], and N_2 [21]. Zhang et al. [22] compared the effect of different aerobic and anaerobic atmospheres, as well as a vacuum on defect formation during the debinding of alumina parts. Vacuum minimized the number of defects in the bodies after debinding and provided a higher sintered density. Another study by Wu et al. [23] confirmed a higher sintered density of alumina ceramics after debinding in a vacuum compared with debinding in air. Zhou et al. [24] proposed a two-step process involving vacuum debinding followed by air debinding. Vacuum debinding prevented abrupt gas formation, and subsequent air debinding removed all remaining carbon residues. However, most of these articles only provided a limited explanation of the effect of debinding atmospheres. Discussion of the underlying mechanisms of debinding in different atmospheres was either absent, or the explanation was not supported by adequate microstructural observations [17,18].

The objective of this investigation was to describe the effect of different heating profiles and debinding atmospheres on the size limit for defect-free binder removal from bodies printed using the DLP method. Specifically, the objective was to identify and explain the main differences in debinding mechanisms in air and inert atmospheres and to correlate these mechanisms with the maximum attainable size of the defect-free bodies after debinding.

2. Experimental

2.1. 3D printing of test bodies

The alumina bodies were prepared using a DLP printer (CeraFab S65, Lithoz GmbH, Austria) and a commercially available photocurable alumina suspension (Lithalox 350, Lithoz GmbH, Austria). The test bodies were printed as cylinders with constant heights of 15 mm and diameters of 5 mm, 9 mm, 11 mm, and 15 mm. Printing was performed with an exposure energy of 150 mJ cm^{-2}, a layer thickness of 25 μm, and a light intensity of 50 mW cm^{-2}. The system provides a lateral pixel resolution of 40 × 40 $μm^2$, enabling the production of ceramic bodies with high dimensional accuracy and surface quality. All printing parameters were selected based on the manufacturer's recommendations for the material to ensure optimal printing and curing behavior. After printing, a thin layer of uncured material suspension remains on the surface of the green body, making subsequent cleaning essential prior to thermal post-treatment and sintering into dense ceramic. For consistency, all printed test specimens were cleaned in the same manner, using an airbrush with a commercially available cleaning solvent (LithaSol 20, Lithoz GmbH, Austria), followed by drying with pressurized air.

2.2. Thermal analysis of printed bodies

Thermogravimetric analysis (TGA) and differential thermal analysis (DTA) of the printed bodies were performed using a TGA/DTA analyzer (96 Line TGA - DTA/DSC, Setaram, France) at a heating rate of 1 °C min^{-1} up to a temperature of 800 °C in nitrogen and air (80 % N_2+20 % O_2) atmospheres with a gas flow of 50 ml min^{-1}. Three sizes of samples were tested: a crushed sample (crushed in a mortar), a small sample (body volume of ~45 mm^3), and a large sample (body volume of ~90 mm^3). The samples were cut from the largest printed cylinder.

2.3. Debinding and sintering of cylindrical test bodies

The samples used for the binder removal were printed without any additional pretreatment before debinding. Debinding experiments were performed in both an air and a nitrogen atmosphere. For air debinding, the ceramic bodies were placed on a ceramic plate. Air debinding was performed in a static atmosphere. For nitrogen debinding, the bodies were embedded in granular activated carbon (AY-5 12 ×30, Carbon Link, UK). A nitrogen flow rate of 20 L h^{-1} was maintained during the binder removal in the muffle furnace. Two debinding schedules with different heating rates (long and short) were applied, as shown in Fig. 1 (a). The long schedule in the air atmosphere was recommended by the producer of the ceramic suspension for large bodies. Both debinding schedules were tested in both air and nitrogen atmospheres, i.e., four variants of debinding experiments were conducted. Ten samples of each size were used for each debinding experiment. After debinding, all samples were sintered in air at 1650 °C using the schedule given in Fig. 1 (b).

In addition, the debinding of cylinders with a diameter of 15 mm using the short debinding schedule in nitrogen or air atmospheres was interrupted at various temperatures (150 °C, 200 °C, 250 °C, 300 °C, and 350 °C) to examine their internal structure and monitor the progress of binder removal.

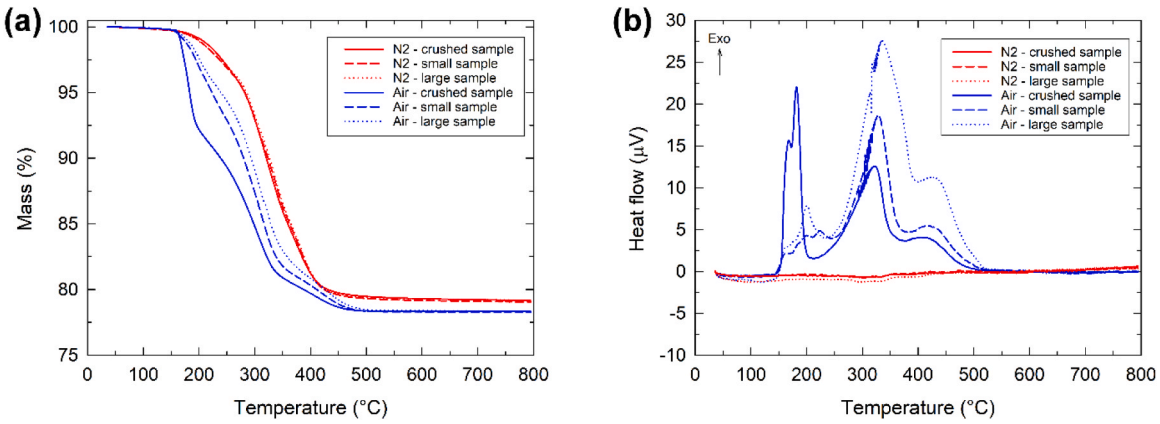

Fig. 2. Thermal analysis of the printed samples showing (a) thermogravimetric curves and (b) heat flow curves.

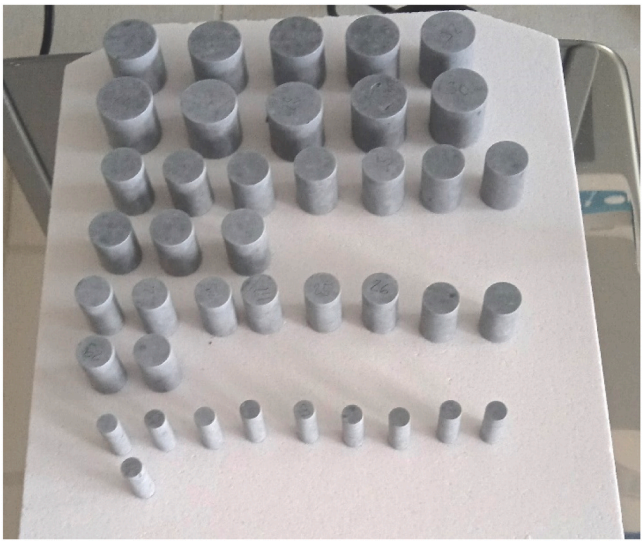

Fig. 3. Set of printed cylinders after debinding in a nitrogen atmosphere.

Table 1
Relative sintered density and percentage of defect-free sintered bodies after debinding in nitrogen.

N_2	Long debinding schedule			Short debinding schedule		
Cylinder diameter (mm)	Relative density (% t.d.)	SD* (% t. d.)	Defect-free (%)	Relative density (% t.d.)	SD* (% t. d.)	Defect-free (%)
5	97.58	0.13	100	97.28	0.18	100
9	95.98	0.20	100	96.06	0.18	100
11	95.55	0.10	100	95.51	0.18	100
15	94.42	0.22	100	94.67	0.25	80

* SD = sample standard deviation of relative density

Table 2
Relative sintered density and percentage of defect-free sintered bodies after debinding in air.

Air	Long debinding schedule			Short debinding schedule		
Cylinder diameter (mm)	Relative density (% t.d.)	SD* (% t. d.)	Defect-free (%)	Relative density (% t.d.)	SD* (% t. d.)	Defect-free (%)
5	97.31	0.24	100	97.40	0.31	80
9	96.33	0.19	70	96.66	0.23	0
11	96.03	0.34	20	96.26	0.24	0
15	95.50	0.40	0	95.55	0.32	0

* SD = sample standard deviation of relative density

2.4. Characterization methods

Macro defects and cracks in the printed samples were checked using an optical microscope before and after debinding. After sintering, the samples were inspected optically again, and their density was measured in water using the Archimedes method. Relative densities were calculated using a theoretical density (t.d.) of 3.987 g cm^{-3} for alumina. The macrostructure of the samples after partial debinding was analyzed using a stereomicroscope (Stemi 508, Zeiss, Germany) on polished cross sections. The microstructure of the green bodies, the bodies after partial debinding, and the sintered bodies was analyzed using a scanning electron microscope (SEM) (Verios 460 L, FEI, Czech Republic). For the SEM investigation of the as-printed samples and the samples after partial debinding, the cross section of the samples was ion beam polished under cryogenic conditions (-120 °C, 6 kV, 3 mA) using an ion beam milling system (EM TIC 3X, Leica, Germany). The sintered samples were mechanically polished. All samples for electron microscopy were carbon-coated with 15 nm of carbon (AM ACE 600, Leica, Germany).

3. Results

3.1. Thermal analysis

Fig. 2(a) shows the mass loss of the printed bodies during heating in nitrogen and air atmospheres. The presence of oxygen in the air atmosphere shifted the mass loss curves to lower temperatures compared to the nitrogen atmosphere. A pronounced effect of sample size was observed during debinding in the air. The mass loss curves of larger samples were moved to higher temperatures, closer to the mass loss curves of samples treated in nitrogen. On the other hand, only negligible differences were found between samples of different sizes during debinding in nitrogen. After debinding in the nitrogen atmosphere, carbon residues from the organic binder and other additives (approximately 1 % of the total mass) remained in the body structure. Fig. 2(b) presents the thermal effect of debinding in different atmospheres. Thermal degradation in nitrogen resulted in minimal thermal effects. Conversely, the oxidative degradation occurring in air exhibited three exothermic peaks. These peaks correspond to the steps with steep mass losses (see Fig. S1). As the sample size increased, the mass loss below 200 °C decreased rapidly, as did the first low-temperature exothermic peak. The other two exothermic peaks increased as the mass loss shifted to higher temperatures in the larger sample.

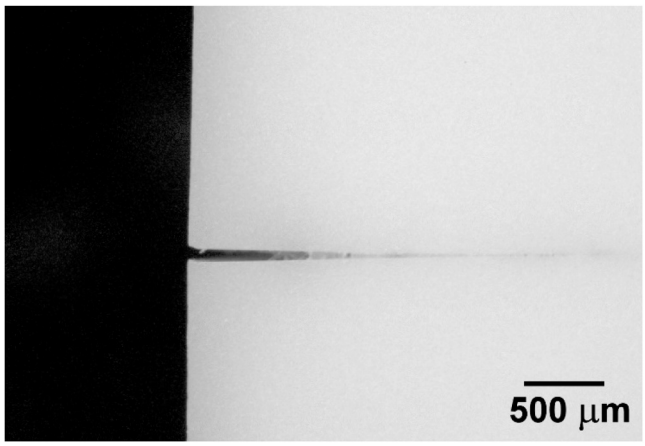

Fig. 4. Cross-section detail of a sintered cylinder showing a typical crack after debinding in air.

3.2. Debinding defects

A set of cylindrical bodies with different diameters after debinding in nitrogen is shown in Fig. 3. Tables 1 and 2 show the percentage of defect-free bodies after debinding in nitrogen and air, respectively. It is obvious that debinding in the nitrogen atmosphere was more successful than in the air atmosphere. Debinding in nitrogen using the long schedule provided all bodies defect-free. Debinding in nitrogen using the short schedule also provided defect-free bodies, except for the largest cylinders with a diameter of 15 mm. On the other hand, debinding in the air was completely successful only when using the long schedule for cylinders with a diameter of 5 mm. In all other cases, cracks appeared in several or often in all of the samples. The typical debinding defect is shown in Fig. 4. It was a partial or full crack through the cylindrical sample along the printing layers. Tables 1 and 2 also show the relative densities of sintered ceramic bodies. The sintered densities were similar for bodies processed in nitrogen using long and short debinding schedules, decreasing from 97.6 % t.d. to 94.4 % t.d. with increasing cylinder diameter. The densities of bodies processed in air were similar to those processed in nitrogen. The slightly higher densities achieved in larger cylinders processed in air compared to nitrogen could result from cracking. Fully cracked parts behaved as smaller, individual bodies during the remaining debinding and sintering and reached a density corresponding to that of the smaller bodies.

3.3. Structure characterization

Fig. 5 shows photographs of longitudinal and transverse sections of cylindrical bodies with a diameter and height of 15 mm after debinding to different temperatures in nitrogen and air. The cutting scheme used for sample preparation is shown in Fig. S2. Clear differences can be observed between the longitudinal and transverse sections of the bodies treated in nitrogen (Fig. 5(a)) and air (Fig. 5(b)). In the nitrogen atmosphere, the bodies turned slightly gray homogeneously throughout the entire volume during debinding. Debinding in air resulted in the formation of a brownish-gray layer of oxidative degradation products, which extended from the surface toward the center of the bodies as the debinding temperature increased. Additionally, the photos of the transverse sections of the cylindrical bodies show that the binder degradation and removal were microscopically inhomogeneous, i.e., inhomogeneity in the debinding process was observed within the volume of the individual printed layer. Because the transverse cut was not perfectly perpendicular to the cylinder axis (i.e., not perfectly parallel with the printed layers), it intersected several printed layers. Color strips that appeared on the cut surface demonstrated cross sections of individual printed layers with more or less degraded areas. This phenomenon was clearly observed during air debinding due to the brownish-gray degradation products. These strips were also observed to a less pronounced extent in bodies treated in nitrogen. The graph in Fig. 6 shows the binder loss of the investigated cylindrical bodies (with 15 mm in diameter) in different atmospheres. The air atmosphere sped up the binder removal compared to the nitrogen atmosphere. To compare structures with the same binder loss in air and nitrogen, bodies must be heated to different temperatures, e.g., the binder loss of ~40 % was reached at a temperature of 250 °C in air and 300 °C in nitrogen.

To better understand the debinding mechanisms, we investigated the

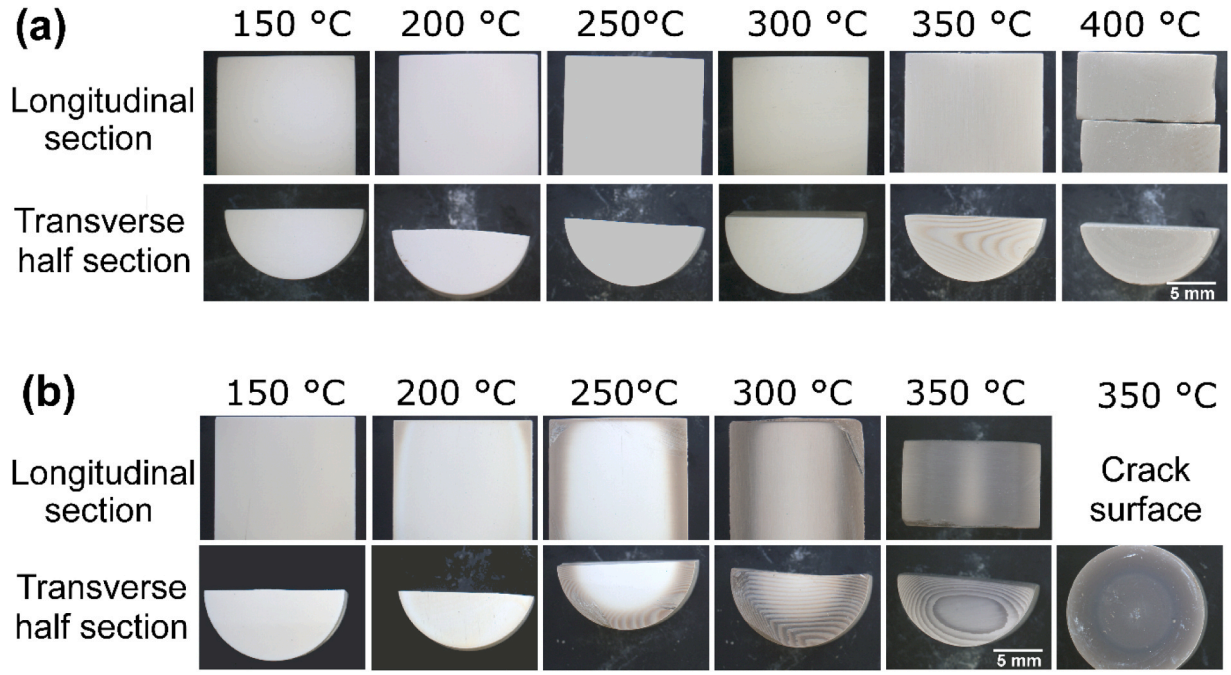

Fig. 5. Longitudinal and transverse sections of cylindrical bodies with a diameter and height of 15 mm after debinding to different temperatures in (a) nitrogen and (b) air using the short schedule.

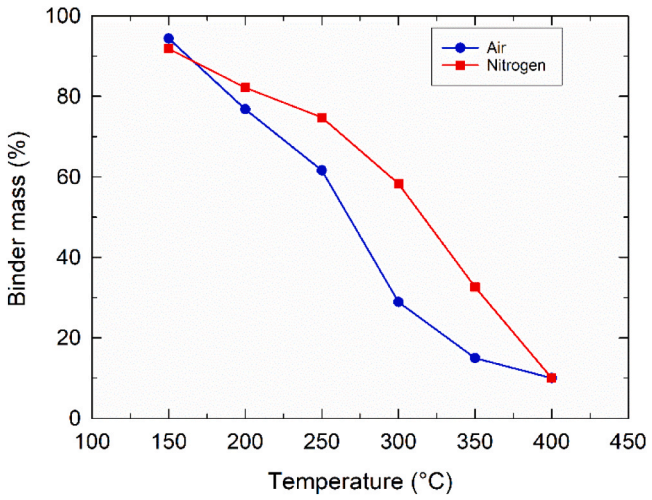

Fig. 6. Binder mass loss during debinding of cylindrical bodies with a diameter and height of 15 mm after debinding to different temperatures in nitrogen and air.

microstructure of the bodies after partial debinding. Fig. 7 shows the microstructure of printed green bodies, which can serve as a standard for comparison with bodies after partial binder removal. Fig. 7(a) shows a cross-section of a green body with printed layers of 25 μm in thickness. The interfaces between the layers are clearly observed, indicating that they created a certain structural inhomogeneity in the body. Fig. 7(b) shows a detailed view of the microstructure. White arrows mark the interface between the printed layers. The printed layers consisted of dispersed ceramic particles and a binder that fully filled the pores between the particles. Discontinuity in the regular particle packing was observed at the interface between the layers, though no voids or air bubbles were present. Fig. 8 shows the microstructure of a body after debinding to 250 °C in an air atmosphere (with a binder loss of ~40 %). A porous structure with a porosity gradient in the printed layer was found near the surface of the body (see Fig. 8(a)). The difference in the porosity was visible at the interface of the printed layers. A similar structure, but with a smaller overall porosity, could also be found in the center of the body (see Fig. 8(c)). However, a substantially reduced porosity was found in the microstructure near the edge of the brownish-gray layer (see Fig. 8(b)). The porosity at this position decreased through the printed layer from a moderate porosity to an almost fully dense structure, similar to the printed green bodies. An important finding from these observations is that the overall porosity at the edge of the brownish-gray layer was likely lower than that in the center of the body.

The structure of the body after debinding in air to 250 °C can be compared with the structure of a body after debinding in nitrogen. Fig. 9 shows the microstructure of the body after debinding to 250 °C in nitrogen. Binder loss was lower in nitrogen than in air (25 % vs. 40 %). This structure resembled that of printed green bodies, but had several isolated pores. An apparent porosity gradient was present between the surface and the center of the body, as well as inside the individual printed layers. In contrast to air, no intermediate structure was observed. Fig. 10 shows the microstructure of the body after debinding to 300 °C in nitrogen. After debinding at this temperature in nitrogen, we obtained the binder loss similar to that in air debinding to 250 °C (~40 %). The SEM images reveal a porous structure with no apparent difference in porosity between the surface and the center of the body. The porosity gradient inside the individual layers also decreased substantially. In all debinding cases, we found that the least porous part of the printed layer (the darker area in the SEM images) was located on the side of the layer surface that was directly exposed to the polymerizing light. After sintering at 1650 °C for 2 h, 2.5–4.5 % of porosity remained in the ceramics, depending on the body size. Nevertheless, no signs of interfaces between layers can be observed (see Fig. S3).

4. Discussion

The oxidative degradation of organic polymers has a lower activation energy than thermal degradation and can be active at lower temperatures [16]. Therefore, the mass loss in air can occur at lower temperatures than in nitrogen, where only thermal degradation occurs. However, oxygen from the air must diffuse into the organic binder during the oxidative degradation, and the products of the oxidative degradation must diffuse out of the body to evaporate. The increasing diffusion path limits the extent of oxidative degradation toward the center of the body. Thus, the decreasing specific surface area of larger samples reduces the contribution of oxidative degradation to the total mass loss during debinding, as illustrated in Fig. 2. Furthermore, the oxidative degradation of the binder system occurs in several steps (see Fig. S2) through stable intermediate products [25]. The brownish-gray layer growing from the surface to the center of the body represents the formation of the stable intermediate products of oxidative degradation (see Fig. 5). These oxidative intermediate products remain embedded in the structure and especially at the edge of the brownish-gray layer "seal" the structure, as shown in Fig. 8(b). Further oxidation and removal of these stable intermediate products only occur at temperatures between 300 °C and 350 °C (see Fig. 2). At this temperature, however, thermal degradation is already active throughout the entire body. We hypothesize that the stable oxidative intermediate products inside the body prevent the diffusion of emerging volatile products of the thermal degradation (and other possible low molecular

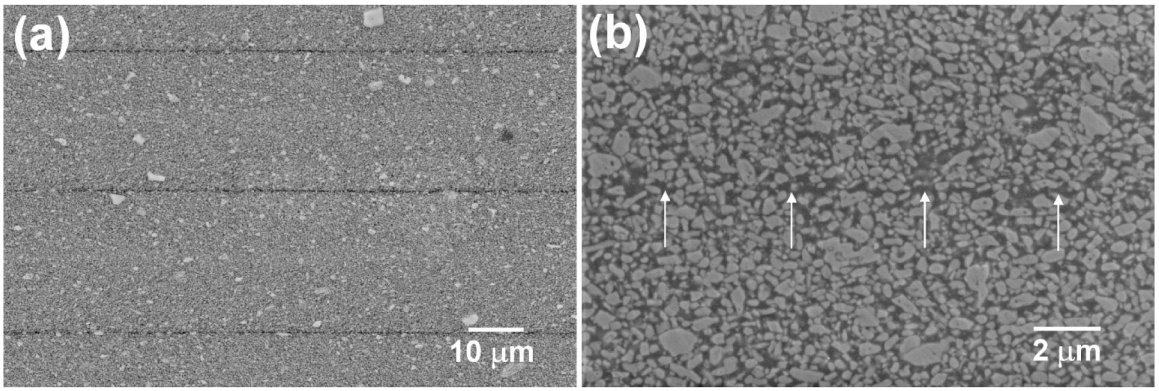

Fig. 7. SEM micrographs of (a) a cross section of a green body with printed layers and (b) the detailed microstructure of a green body. The arrows indicate the interface between printed layers. The image in Fig. 7(a) was acquired in backscattered electron mode, and the image in Fig. 7(b) was acquired in secondary electron mode.

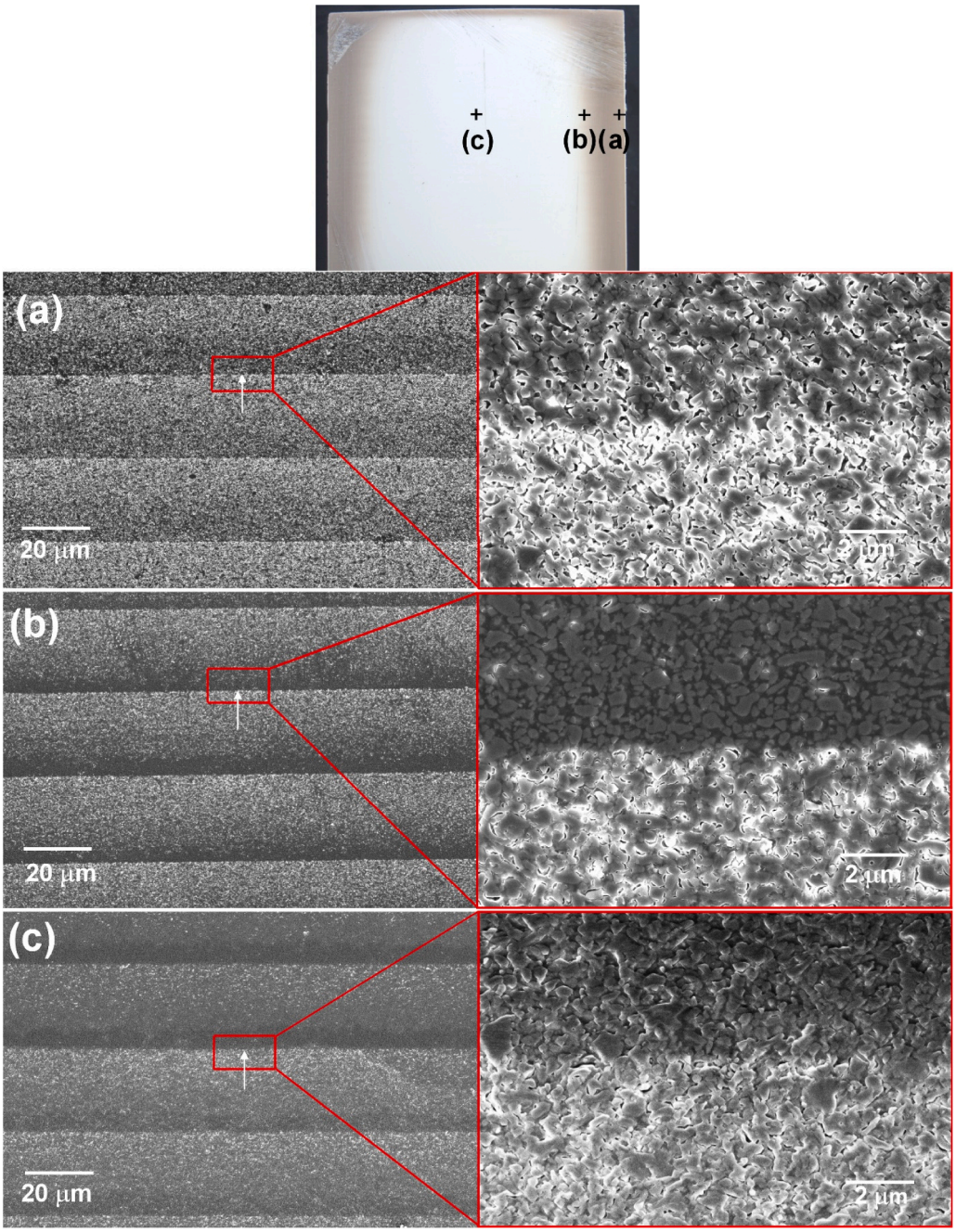

Fig. 8. SEM micrographs of the body structure after debinding to 250 °C in air, taken (a) near the surface, (b) at the edge of the brownish-grey layer, and (c) in the center of the body. The accompanying optical photograph shows the exact position of the observed microstructures in the body cross section. The arrow indicates the direction of the incident light during the printing of individual layers.

weight binder components) to the surface and their subsequent evaporation. Thermal degradation products thus gasify inside the body, and the gas pressure causes cracks along the layer interfaces, which are the weakest points of the body. The present research suggests that air debinding can be beneficial for thin-walled bodies (< 5 mm) because it accelerates binder removal. However, it is not suitable for thicker-walled bodies due to the formation of cracks. In a nitrogen atmosphere, the maximum defect-free wall thickness depends on the ability of the low molecular degradation products to diffuse to the body surface (or to the nearest binder/atmosphere interface) and evaporate. This diffusion must be quick enough to prevent the accumulation of a critical concentration of low molecular weight degradation products, which could result in boiling and gas evolution inside the body. Quick diffusion of degradation products can be supported by the formation of a porous structure. Low molecular components that are not involved in the photopolymerization reaction (e.g., non-reactive diluents or unreacted monomers) can be removed before the main decomposition of the polymeric network. The removal of these low molecular components can facilitate the formation of pores and interconnected channels, thus providing shorter pathways for the subsequent discharge of degradation products from the decomposed polymer network.

The proposed debinding mechanism resembles the binder removal process described in bodies with multicomponent thermoplastic binders [26–28]. The main difference lies in the crosslinked structure of the polymer binder in 3D printed bodies. Unlike the viscous polymer melts in thermoplastic ceramic mixtures, binder redistribution is limited

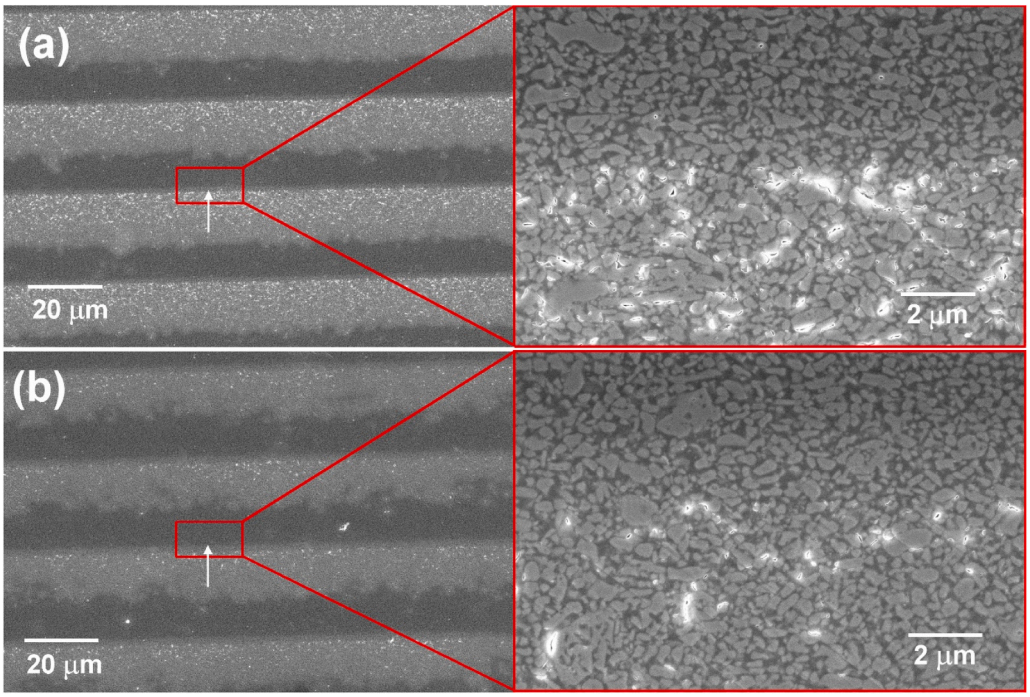

Fig. 9. SEM micrographs of the body structure after debinding to 250 °C in nitrogen, taken (a) near the surface and (b) in the center of the body. The arrow indicates the direction of the incident light during the printing of individual layers.

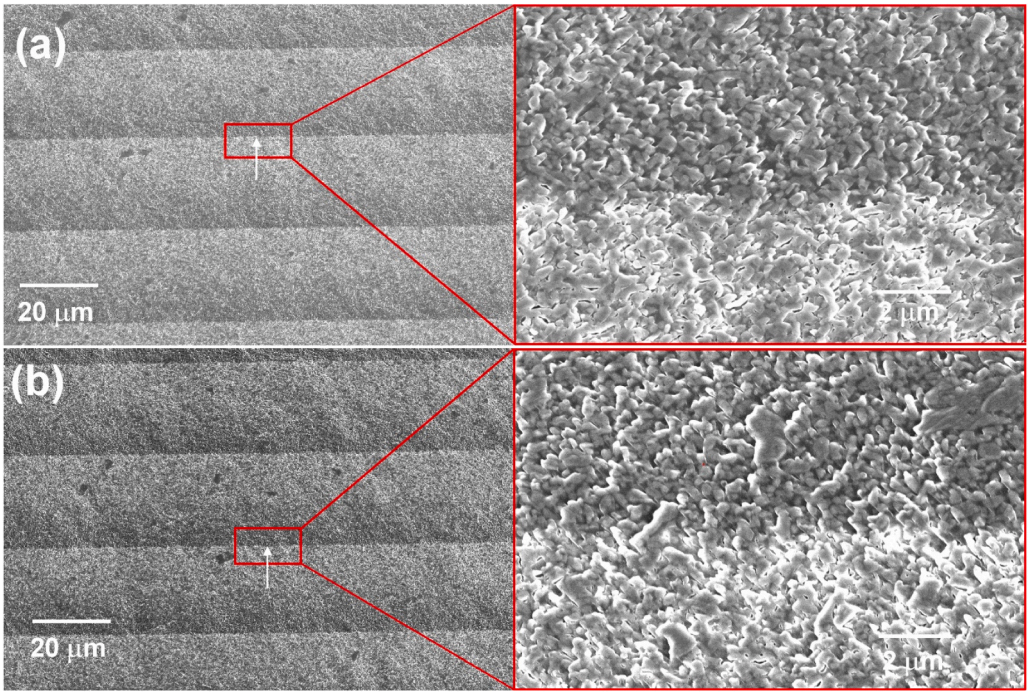

Fig. 10. SEM micrographs of the body structure after debinding to 300 °C in nitrogen, taken (a) near the surface and (b) in the center of the body. The arrow indicates the direction of incident light during the printing of individual layers.

during debinding in 3D printed bodies. One of the key features of the thermal removal of crosslinked binders from 3D printed bodies is the formation of closed pores in a fully saturated structure in the body center, as confirmed in the microstructure images in Fig. 9. This phenomenon is highly unfavorable in structures with viscous polymer melts [29]. It can be expected that the pore formation inside the saturated body can accelerate the transport of low molecular components to the body surface, especially once the pores become interconnected. Another unique feature of the present printed bodies is the porosity inhomogeneity in the individual printed layers during debinding. It is supposed that the surface of the layer exposed to the polymerizing light undergoes the highest polymer conversion, i.e., the highest crosslinking density. The light energy and, thus, the degree of polymer conversion decrease exponentially with the distance from the light-exposed surface [30]. This results in a different crosslinking density throughout the layer. A lower crosslinking density results in a higher amount of

unreacted monomers. These low molecular components (unreacted monomers and other low molecular binder components) can more easily diffuse through the less crosslinked structure to the surface, creating pores before the crosslinked polymer network undergoes massive thermal degradation. Once thermal degradation of crosslinked polymer network is initiated, the porosity inhomogeneity in the printed layer diminishes and finally disappears (see Fig. 10). While the individual printed layers and their interfaces played an important role in the binder removal, this inhomogeneity was eliminated during sintering, and a fully homogeneous and isotropic microstructure was obtained, as shown in Fig. S3.

5. Conclusions

This study investigated the influence of the debinding atmosphere and heating schedule on defect formation during the thermal debinding of alumina bodies fabricated using the digital light processing method. The results showed that the maximum size of a defect-free body depends strongly on the debinding atmosphere. The nitrogen atmosphere allowed for successful debinding of parts up to 15 mm in diameter, while the air atmosphere limited defect-free debinding to samples of 5 mm. Crack formation in air was attributed to the oxidative degradation of the binder, which proceeded from the surface to the center of the body and produced stable intermediates that hindered uniform binder removal. Prolonging the heating schedule increased the maximum size of defect-free bodies, though it could not fully counteract the effects of oxidative degradation. The structure and density of sintered bodies were not affected by the binder removal conditions.

CRediT authorship contribution statement

Premysl Stastny: Writing – original draft, Methodology, Investigation, Formal analysis, Conceptualization. **Ondrej Man:** Methodology, Formal analysis. **Dominik Brouczek:** Validation, Investigation. **Martin Schwentenwein:** Validation, Investigation. **Martin Trunec:** Writing – review & editing, Writing – original draft, Supervision, Methodology, Investigation, Conceptualization.

Declaration of Competing Interest

The authors declare that they have no known competing financial interests or personal relationships that could have appeared to influence the work reported in this paper.

Acknowledgments

The research was financially supported by the Ministry of Education, Youth and Sport of the Czech Republic (MEYS CR) under the grant LUC23069 and by the Programme Johannes Amos Comenius under the grant CZ.02.01.01/00/22_008/0004634. We also acknowledge Czech-NanoLab Research Infrastructure supported by MEYS CR (LM2023051).

Appendix A. Supporting information

Supplementary data associated with this article can be found in the online version at doi:10.1016/j.jeurceramsoc.2025.117891.

Data Availability

The relevant article data can be found in the Zenodo.org repository under DOI: 10.5281/zenodo.15646595. The preprint is available at Zenodo.org under the DOI: 10.5281/zenodo.15640989.

References

[1] A. Zocca, P. Colombo, C.M. Gomes, J. Günster, Additive manufacturing of ceramics: issues, potentialities, and opportunities, J. Am. Ceram. Soc. 98 (2015) 1983–2001.
[2] Z.W. Chen, Z.Y. Li, J.J. Li, C.B. Liu, C.S. Lao, Y.L. Fu, C.Y. Liu, Y. Li, P. Wang, Y. He, 3D printing of ceramics: a review, J. Eur. Ceram. Soc. 39 (2019) 661–687.
[3] Y. Lakhdar, C. Tuck, J. Binner, A. Terry, R. Goodridge, Additive manufacturing of advanced ceramic materials, Prog. Mater. Sci. 116 (2021) 100736.
[4] F. Zhang, L.Y. Zhu, Z.A. Li, S.Y. Wang, J.P. Shi, W.L. Tang, N. Li, J.Q. Yang, The recent development of vat photopolymerization: a review, Addit. Manuf. 48 (2021) 102423.
[5] S.A. Rasaki, D.Y. Xiong, S.F. Xiong, F. Su, M. Idrees, Z.W. Chen, Photopolymerization-based additive manufacturing of ceramics: a systematic review, J. Adv. Ceram. 10 (2021) 442–471.
[6] S. Zakeri, M. Vippola, E. Levänen, A comprehensive review of the photopolymerization of ceramic resins used in stereolithography, Addit. Manuf. 35 (2020) 101177.
[7] M. Canillas, F. Jean, A. Thuault, D. Hautcoeur, A. Leriche, Microwave-assisted debinding of Al2O3 parts printed by stereolithography, Ceram. Int 49 (2023) 18343–18352.
[8] H. Li, Y. Liu, Y. Liu, K. Hu, Z. Lu, J. Liang, Effects of solvent debinding on the microstructure and properties of 3D-printed alumina ceramics, ACS Omega 5 (2020) 27455–27462.
[9] N. Nurmi, E. Frankberg, M. Rinne, T. Sandblom, P. Konnunaho, E. Levanen, Enabling fast debinding of ceramic vat photopolymerization prints with supercritical carbon dioxide as a solvent, Addit. Manuf. 84 (2024) 104143.
[10] S.X. Zhou, G.Z. Liu, C.S. Wang, Y. Zhang, C.Z. Yan, Y.S. Shi, Thermal debinding for stereolithography additive manufacturing of advanced ceramic parts: a comprehensive review, Mater. Des. 238 (2024) 112632.
[11] A.K. Hofer, J. Rabitsch, D. Jutrzenka-Trzebiatowska, C. Hofstetter, I. Gavalda-Velasco, J. Schlacher, M. Schwentenwein, R. Bermejo, Effect of binder system on the thermophysical properties of 3D-printed zirconia ceramics, Int J. Appl. Ceram. Tec. 19 (2022) 174–180.
[12] E. Schwarzer-Fischer, J. Abel, J. Sieder-Katzmann, M. Propst, C. Bach, U. Scheithauer, A. Michaelis, Study on CerAMfacturing of novel alumina aerospike nozzles by lithography-based ceramic vat photopolymerization (CerAM VPP), Materials 15 (2022) 3279.
[13] T. Marie, Z. Du, Ch.L. Gan, S. Marinel, V.S. Sridharan, Ch Maniere, Debinding and sintering optimization of stereolithography based silicon parts for attaining centimetric wall-thickness shapes, J. Eur. Ceram. Soc. 45 (2025) 116911.
[14] M. Trunec, J. Cihlar, Removal of thermoplastic binders from ceramic green bodies, Ceram. Silik. 41 (1997) 67–80.
[15] J.A. Lewis, Binder removal from ceramics, Annu Rev. Mater. Sci. 27 (1997) 147–173.
[16] J.K. Wright, J.R.G. Evans, Kinetics of the oxidative degradation of ceramic injection molding vehicle, J. Mater. Sci. 26 (1991) 4897–4904.
[17] K. Wang, M.B. Qiu, C. Jiao, J.J. Gu, D.Q. Xie, C.J. Wang, X.B. Tang, Z. Wei, L. D. Shen, Study on defect-free debinding green body of ceramic formed by DLP technology, Ceram. Int 46 (2020) 2438–2446.
[18] J. Kim, C.W. Gal, Y.J. Choi, H. Park, S.Y. Yoon, H.S. Yun, Effect of non-reactive diluent on defect-free debinding process of 3D printed ceramics, Addit. Manuf. 67 (2023) 103475.
[19] J.X. Sun, J. Binner, J.M. Bai, 3D printing of zirconia via digital light processing: optimization of slurry and debinding process, J. Eur. Ceram. Soc. 40 (2020) 5837–5844.
[20] Y.R. Shen, Y. Sun, B.C. Jin, M. Li, B.H. Xing, Z. Zhao, Effect of debinding and sintering profile on the optical properties of DLP-3D printed YAG transparent ceramic, Ceram. Int 48 (2022) 21134–21140.
[21] P.L.A. Alves, I.L. Camargo, J.R. Verza, A.P. Luz, Impact of debinding atmosphere and sintering additives on the fabrication of alumina ceramics via vat photopolymerization, Ceram. Int 51 (2025) 9063–9072.
[22] L. Zhang, J. Huang, Z. Xiao, K. Liu, B. He, B. Xiang, J. Zhai, L. Kong, Effects of debinding conditions on microstructure and densification of alumina ceramics with photopolymerization-based additive manufacturing technology, Ceram. Int 48 (2022) 14026–14038.
[23] H.D. Wu, Y.L. Cheng, W. Liu, R.X. He, M.P. Zhou, S.H. Wu, X. Song, Y. Chen, Effect of the particle size and the debinding process on the density of alumina ceramics fabricated by 3D printing based on stereolithography, Ceram. Int 42 (2016) 17290–17294.
[24] M.P. Zhou, W. Liu, H.D. Wu, X. Song, Y. Chen, L.X. Cheng, F.P. He, S.X. Chen, S. H. Wu, Preparation of a defect-free alumina cutting tool via additive manufacturing based on stereolithography - optimization of the drying and debinding processes, Ceram. Int 42 (2016) 11598–11602.
[25] R.T. Conley, P.L. Valint, Oxidative degradation of poly(ethyl acrylate), J. Appl. Polym. Sci. 9 (1965) 785–797.
[26] M. Trunec, J. Cihlar, Thermal debinding of injection moulded ceramics, J. Eur. Ceram. Soc. 17 (1997) 203–209.
[27] M. Trunec, J. Cihlar, Thermal removal of multicomponent binder from ceramic injection mouldings, J. Eur. Ceram. Soc. 22 (2002) 2231–2241.

[28] M. Trunec, J. Cihlar, S. Diethelm, J. Van Herle, Tubular $La_{0.7}Ca_{0.3}Fe_{0.85}Co_{0.15}O_{3-\delta}$ perovskite membranes, part I: preparation and properties, J. Am. Ceram. Soc. 89 (2006) 949–954.

[29] M.J. Cima, J.A. Lewis, A.D. Doevoe, Binder distribution in ceramic greenware during thermolysis, J. Am. Ceram. Soc. 72 (1989) 1192–1199.

[30] J.W. Halloran, Ceramic stereolithography: additive manufacturing for ceramics by photopolymerization, Annu Rev. Mater. Res. 46 (2016) 19–40.